Azimuthal asymmetries in *D*-meson and jet production at the EIC

Khatiza Banu,[1,2,*] Asmita Mukherjee,[1,†] Amol Pawar,[1,‡] and Sangem Rajesh[3,§]

[1]*Department of Physics, Indian Institute of Technology Bombay, Mumbai-400076, India*
[2]*Center for Frontiers in Nuclear Science, Stony Brook University, Stony Brook, New York 11794-3800, USA*
[3]*Department of Physics, School of Advanced Sciences, Vellore Institute of Technology, Vellore, Tamil Nadu 632014, India*

(Received 4 July 2023; accepted 21 July 2023; published 4 August 2023)

We study the azimuthal asymmetries in back-to-back leptoproduction of the D meson and jet to probe the gluon TMDs in an unpolarized and transversely polarized electron-proton collision at the kinematics of electron-ion collider (EIC). We give predictions for unpolarized cross sections within the TMD factorization framework. In D-meson and jet formation, the only leading order contribution comes from the photon gluon fusion process. We give numerical estimates of the upper bound on the azimuthal asymmetries with the saturation of positivity bounds; also, we present the asymmetries using a Gaussian parametrization of TMDs. We obtain sizable asymmetries in the kinematics that will be accessible at EIC.

DOI: 10.1103/PhysRevD.108.034005

I. INTRODUCTION

Transverse momentum dependent parton distribution functions (TMDs) have become the primary focus of research in hadron physics, as they encode the three-dimensional structure of a hadron. TMDs depend on the parton's longitudinal momentum fraction (x) and its intrinsic transverse momentum ($\boldsymbol{k}_\perp$). In contrast to the collinear parton distribution functions (PDFs), which can only provide one-dimensional tomography of the hadron since they are dependent only on the parton's longitudinal momentum fraction, the TMDs give a three-dimensional momentum space description of the hadron in terms of its constituents. TMDs are typically nonperturbative in nature [1], and they can be studied in processes like the semi-inclusive deep inelastic scattering process (SIDIS) [2,3] and Drell-Yan (DY) [4,5]. In these processes, one observes a final hadron with transverse momentum or a lepton pair that contains the footprint of the transverse momentum of the partons inside the proton. TMDs are not universal, since their operator definition contains a gauge link (Wilson line), making them process dependent [6]. Unlike quark TMDs, which only need one gauge link to be defined in a gauge-invariant way, the gluon TMD operators require two gauge links, which depend on the process being considered. These gauge links could either be future-pointing gauge links (final state interactions) or past-pointing gauge links (initial state interactions) or a mixture of both. In small-x physics, these two types of TMDs (known as unintegrated gluon distributions) are known as the Weizsäcker-Williams (WW) gluon distribution [7,8] and the dipole gluon distribution [9]. Both of these distributions have been commonly used in the literature and can be studied in different processes depending on the process-dependent gauge link structure.

At the leading twist, there are eight gluon TMDs. Among these, the Boer-Mulders function, $h_1^{\perp g}$, and the Sivers function, $f_{1T}^{\perp g}$, have gained a lot of attention in recent years. Similar to this, we have quark TMDs, and the quark Sivers function is fairly well-known thanks to relentless experimental and theoretical efforts [10–12]. However, little is known about the gluon TMDs. The linearly polarized gluon distribution was first discussed in [13] and calculated in a model in [14]. The Boer-Mulders TMD represents the density of linearly polarized gluons inside an unpolarized proton. The $h_1^{\perp g}$ is a T (time-reversal) and chiral-even function; hence, it is nonzero even in the absence of initial-state interactions (ISI) or final-state interactions (FSI) [13]. More information about the linearly polarized gluon TMDs can be obtained by calculating the $\cos 2\phi_T$ type of azimuthal asymmetry, which is a ratio of linearly polarized gluon TMD to unpolarized gluon TMD. The gluon Sivers function describes the distribution of unpolarized gluons inside a transversely polarized hadron.

*banu2765@iitb.ac.in
†asmita@phy.iitb.ac.in
‡194120018@iitb.ac.in
§sangem.rajesh@vit.ac.in

The correlation between the intrinsic transverse momentum of a parton and polarization of a proton leads to the asymmetric distribution of final-state particles, which is the so-called Sivers asymmetry [15,16]. Sivers asymmetry helps in understanding the spin crisis [17]. The first transverse moment of the Sivers function is related to the twist-three Qiu-Sterman function [18,19]. The $f_{1T}^{\perp g}$, T-odd, changes sign in the SIDIS process compared to that in the DY process [20]. The ISI and FSI play an important role in the Sivers asymmetry; in general, the gluon Sivers function (GSF) can be expressed in terms of two independent GSFs that are called f-type and d-type GSF, respectively [20–24]. The f-type GSF contains ($++$ or $--$) gauge link and in the literature of small-x physics is called as Weizsacker-Williams (WW) gluon distribution. The d-type GSF contains a ($+-$) gauge link and is called dipole-type gluon distribution. The nonzero quark Sivers function has been extracted from the HERMES [25,26] and COMPASS [27,28] experiments, but the gluon Sivers function remains unknown, although initial attempts have been made [29,30] to extract the GSF from RHIC data [31] in the midrapidity region.

Theoretical investigations indicate that the gluon TMDs could be probed in the production of heavy-quark pair or dijet [32–34], J/ψ-photon [35], and J/ψ-jet [36–38] at the electron-ion collider (EIC), where the transverse momentum imbalance of the pair is measured. Azimuthal asymmetries have been studied in various processes, including the production of J/ψ [39–43], photon pair [44], and Higgs boson-jet [45] production at LHC that have been proposed to probe the gluon TMDs. In these processes, the transverse momentum of the pair (q_T) is smaller than the individual transverse momentum ($K_\perp$), which allows us to use the TMD factorization. Transverse single-spin asymmetry (SSA) has been studied for inclusive D-meson production both in electron-proton [46] and proton-proton [47–49] collision processes within the generalized parton model framework. The SSA in the electroproduction of the D meson has been studied within the twist-three approach using the collinear factorization framework [50].

In the present article, we present a calculation of azimuthal asymmetries in back-to-back electroproduction of a D meson and jet in the process $e + p \to e + D + \text{jet} + X$ within a TMD factorization framework. We consider the cases where the proton is unpolarized as well as transversely polarized. Our main focus is on calculating the azimuthal asymmetries such as $\cos 2\phi_T$, $\cos 2(\phi_T - \phi_\perp)$, and $\sin(\phi_S - \phi_T)$. These asymmetries allow us to probe linearly polarized gluon TMD and Sivers TMD. In D-meson and jet production, at leading order (LO) in strong coupling constant (α_s), only the partonic channel of virtual photon-gluon fusion, $\gamma^* + g \to c + \bar{c}$, contributes, while the quark channel contributes at next-to-leading order (NLO). At LO, the produced charm quark fragments to form the D meson. and the anticharm quark evolves into the jet. The D meson in the final state is the lightest meson containing a single charm quark (or antiquark). We consider the kinematics where the produced charm and anticharm quarks in the hard process have an almost equal magnitude of transverse momenta, but they are in opposite directions as shown in Fig. 2. The produced D meson (which we assume to be collinear to the fragmenting quark) and jet are almost back to back in the transverse plane. In this kinematical region, the total transverse momentum (q_T) of the system is much smaller than the individual transverse momentum ($K_\perp$) of the outgoing particle; i.e., $|\boldsymbol{q}_T| \ll |\boldsymbol{K}_\perp|$. Only in this region, the intrinsic transverse momentum can have significant effects, and we can assume that the TMD factorization is valid for the given process.

This paper is organized as follows: In Sec. II, we introduce the relevant kinematics of D-meson and jet production in the SIDIS process to calculate the azimuthal asymmetries. In Sec. III, we give the derivation to calculate the unpolarized scattering cross section using TMD factorization. The azimuthal asymmetries that give direct access to gluon TMDs are given in Sec. IV as well as the parametrization of the TMDs. In Sec. V, the numerical results and discussion are given. Finally, we conclude, and an appendix is given at the end.

II. FORMALISM

We start this section by specifying our notation and kinematics of SIDIS. We consider the production of a D-meson and a jet in (un)polarized ep scattering process,

$$e(l) + p^{\uparrow}(P) \to e(l') + D(P_h) + \text{jet} + X. \tag{1}$$

The four-momenta of each particle is given in the round brackets, and the transverse polarization of the proton is represented with an arrow in the superscript. For the collision energy that we are interested in for this work, the process involves one-photon exchange. We define the virtual photon momentum, $q = l - l'$, and its invariant mass as $Q^2 = -q^2$. We have considered the photon-proton center-of-mass (cm) frame, in which the photon and proton move along the z axis. We define the following kinematical variables,

$$s = (l + P)^2, \qquad x_B = \frac{Q^2}{2P \cdot q}, \qquad y = \frac{P \cdot q}{P \cdot l}, \tag{2}$$

where s is the square of the energy of the electron-proton system in the cm frame, Q^2 is the virtuality of the photon, x_B is known as the Bjorken variable, and y is called the inelasticity variable, which is physically interpreted as the fraction of the electron energy transferred to the photon. These variables are related to each other through the relation $Q^2 \approx x_B y s$.

We introduce two lightlike vectors n_+ and n_-, which obey the relations $n_+^2 = n_-^2 = 0$ and $n_+ \cdot n_- = 1$. The

four-momenta of the target system proton P and virtual photon q can be written as

$$P^\mu = n_-^\mu + \frac{M_p^2}{2} n_+^\mu \approx n_-^\mu,$$
$$q^\mu = -x_B n_-^\mu + \frac{Q^2}{2x_B} n_+^\mu \approx -x_B P^\mu + (P\cdot q) n_+^\mu, \quad (3)$$

with $P^2 = 0$. The invariant mass of virtual photon-proton system is defined as $W_{\gamma p}^2 = (q+P)^2$ and can also be expressed as $W_{\gamma p}^2 = \frac{Q^2(1-x_B)}{x_B} = ys - Q^2$, and the mass of the proton is denoted by M_p. We can express all the momenta in terms of $n_-^\mu = P^\mu$ and $n_+^\mu = (q^\mu + x_B P^\mu)/P\cdot q$. The four-momentum of the incoming lepton reads as

$$l^\mu = \frac{1-y}{y} x_B n_-^\mu + \frac{1}{y}\frac{Q^2}{2x_B} n_+^\mu + \frac{\sqrt{1-y}}{y} Q \hat{l}_\perp^\mu, \quad (4)$$

with $l^2 = 0$ and $\hat{l}_\perp^\mu$ is the unit transverse vector.

The LO partonic subprocess $\gamma^*(q) + g(k) \to c(p_1) + \bar{c}(p_2)$ contributes to the process considered above.

In terms of lightlike vectors, the four-momentum of the initial gluon is given as

$$k^\mu \backsimeq x P^\mu + k_{\perp g}^\mu, \quad (5)$$

where, x and $k_{\perp g}$ are, respectively, the light-cone momentum fraction and the intrinsic transverse momentum of the incoming gluon with respect to the parent proton direction. The four momenta of the produced heavy quarks in terms of lightlike vectors are given as

$$p_1^\mu = z_1 (P\cdot q) n_+^\mu + \frac{m_c^2 + \boldsymbol{p}_{1\perp}^2}{2 z_1 P\cdot q} P^\mu + p_{1\perp}^\mu$$
$$p_2^\mu = z_2 (P\cdot q) n_+^\mu + \frac{m_c^2 + \boldsymbol{p}_{2\perp}^2}{2 z_2 P\cdot q} P^\mu + p_{2\perp}^\mu, \quad (6)$$

where $z_1 = \frac{P\cdot p_1}{P\cdot q}$ and $z_2 = \frac{P\cdot p_2}{P\cdot q}$ are the momentum fractions of the charm and anticharm quarks, and m_c is the mass of the produced charm and anticharm quark. The $p_{1\perp}$ and $p_{2\perp}$ are the transverse momenta of charm and anticharm quarks, respectively. The four-momentum of the D meson in terms of lightlike vectors can be written as

$$P_h^\mu = z_h (P\cdot q) n_+^\mu + \frac{m_h^2 + \boldsymbol{P}_{hT}^2}{2 z_h P\cdot q} P^\mu + P_{hT}^\mu. \quad (7)$$

The inelastic variable $z_h = \frac{P\cdot P_h}{P\cdot q}$ is the energy fraction of the virtual photon taken by the observed D meson in proton rest frame, and m_h is the mass of the D meson. The four-momentum of the charm quark, p_1^μ, given in Eq. (6), can be parametrized using the momentum fraction as

$$p_1^\mu = \frac{1}{z} P_h^\mu + \frac{1}{2P\cdot P_h}\left(m_c^2 z - \frac{m_h^2}{z}\right) P^\mu, \quad (8)$$

where $z = \frac{P\cdot P_h}{P\cdot p_1} = \frac{z_h}{z_1}$ is the momentum fraction of D meson in the charm quark frame. Using Eqs. (6) and (8), the transverse momentum of the charm quark and the fragmented D meson are related by the following equation [51],

$$p_{1\perp}^\mu = \frac{1}{z} P_{hT}^\mu. \quad (9)$$

The Mandelstam variables are defined as

$$\hat{s} = (q+k)^2 = -Q^2 + 2q.k,$$
$$\hat{u} = (k - p_1)^2 = m_c^2 - 2k.p_1,$$
$$\hat{t} = (q - p_1)^2 = m_c^2 - Q^2 - 2q.p_1. \quad (10)$$

III. SCATTERING CROSS SECTION

In the ep scattering process, we consider the kinematical region in which the charm and anticharm quarks are produced in a back-to-back configuration. In this kinematics, we use TMD factorization to write the cross section. Here, the total transverse momentum of the system q_T with respect to the lepton plane is small compared to the virtuality of the photon Q and to the mass of D meson m_h. For the total differential scattering cross section for the $e + p \to e + c(p_1) + \bar{c}(p_2) + X$, the process can be written as

$$\mathrm{d}\sigma^{ep\to e+c\bar{c}+X} = \frac{1}{2s}\frac{\mathrm{d}^3\boldsymbol{l}'}{(2\pi)^3 2E_{l'}}\frac{\mathrm{d}^3\boldsymbol{p}_1}{(2\pi)^3 2E_1}\frac{\mathrm{d}^3\boldsymbol{p}_2}{(2\pi)^3 2E_2}$$
$$\times \int \mathrm{d}x\, \mathrm{d}^2\boldsymbol{k}_{\perp g} \mathrm{d}z (2\pi)^4 \delta^4(q + k - p_1 - p_2)$$
$$\times \frac{1}{Q^4} L^{\mu\nu}(l,q) \Phi_g^{\rho\sigma}(x, \boldsymbol{k}_{\perp g}) H_{\mu\rho}^{\gamma^* g\to c\bar{c}}$$
$$\times H_{\nu\sigma}^{*;\gamma^* g\to c\bar{c}} D(z). \quad (11)$$

Here, E_i is the energy of the corresponding particle. In the ep scattering process, the D meson is produced from the fragmentation of produced charm quark. In our kinematics where the D meson and jet are in almost back-to-back configuration, we have neglected the intrinsic transverse momentum of the D meson with respect to the charm quark in the hard part [this can be seen from Eq. (9)], which is small compared to the large transverse momentum $\boldsymbol{P}_{hT}$. In other words, we can consider the D meson to be collinear to the fragmenting heavy quark. This gives the collinear fragmentation function $D(z)$, instead of the TMD fragmentation function in our expression. The differential scattering cross section for the process $e + p \to e + D(P_h) + \bar{c}(p_2) + X$ can be written as [33]

$$d\sigma^{ep\to e+D+\bar{c}+X} = \frac{1}{2s}\frac{d^3\boldsymbol{l}'}{(2\pi)^3 2E_{l'}}\frac{d^3\boldsymbol{P}_h}{(2\pi)^3 2E_h}\frac{d^3\boldsymbol{p}_2}{(2\pi)^3 2E_2} \times \int dx\, d^2\boldsymbol{k}_{\perp g} dz (2\pi)^4 \delta^4(q+k-p_1-p_2) \times \frac{1}{Q^4} L^{\mu\nu}(l,q)\Phi_g^{\rho\sigma}(x,\boldsymbol{k}_{\perp g}) H_{\mu\rho}^{\gamma^* g\to c\bar{c}} \times H_{\nu\sigma}^{*;\gamma^* g\to c\bar{c}} D(z) J(z), \quad (12)$$

where $D(z)$ is the collinear fragmentation function describing the fragmentation of the D meson from the charm quark, and it gives the number density of finding a D-meson inside the charm quark with light-cone momentum fraction z in the charm quark frame.

The invariant phase space of the charm quark is related to the phase space of the final D meson through the Jacobian factor J as

$$\frac{d^3\boldsymbol{p}_1}{E_1} = J(z)\frac{d^3\boldsymbol{P}_h}{E_h} \quad \text{with} \quad J = \frac{1}{z^3}\frac{E_h}{E_1}. \quad (13)$$

The momentum conservation delta function, given in Eq. (11), can be decomposed as follows:

$$\delta^4(q+k-p_1-p_2) = \frac{2}{ys}\delta(1-z_1-z_2)\delta\left(x - \frac{z_2(m_c^2+\boldsymbol{p}_{1\perp}^2)+z_1(m_c^2+\boldsymbol{p}_{2\perp}^2)+z_1z_2Q^2}{z_1z_2ys}\right)\delta^2(\boldsymbol{k}_{\perp g}-\boldsymbol{p}_{1\perp}-\boldsymbol{p}_{2\perp}). \quad (14)$$

After substituting Eq. (9) in Eq. (14), we get

$$\delta^4(q+k-p_1-p_2) = \frac{2}{ys}\delta(1-z_1-z_2)\delta\left(x - \frac{z_2(m_c^2+\boldsymbol{P}_{hT}^2/z^2)+z_1(m_c^2+\boldsymbol{p}_{2\perp}^2)+z_1z_2Q^2}{z_1z_2ys}\right)\delta^2\left(\boldsymbol{k}_{\perp g}-\frac{\boldsymbol{P}_{hT}}{z}-\boldsymbol{p}_{2\perp}\right). \quad (15)$$

The phase space of the outgoing particles is given by

$$\frac{d^3\boldsymbol{l}'}{(2\pi)^3 2E_{l'}} = \frac{1}{16\pi^2}dQ^2 dy, \qquad \frac{d^3\boldsymbol{P}_h}{(2\pi)^3 2E_h} = \frac{d^2\boldsymbol{P}_{hT}dz_h}{(2\pi)^3 2z_h}, \qquad \frac{d^3\boldsymbol{p}_2}{(2\pi)^3 2E_2} = \frac{d^2\boldsymbol{p}_{2\perp}dz_2}{(2\pi)^3 2z_2}. \quad (16)$$

We shift to the coordinate system, which is more suitable for back-to-back scattering, for which we define the sum ($\boldsymbol{q}_T$) and difference of the transverse momenta ($\boldsymbol{K}_\perp$) of the outgoing quark and antiquark as

$$\boldsymbol{q}_T = \frac{\boldsymbol{P}_{hT}}{z} + \boldsymbol{p}_{2\perp}, \qquad \boldsymbol{K}_\perp = \frac{\frac{\boldsymbol{P}_{hT}}{z} - \boldsymbol{p}_{2\perp}}{2}. \quad (17)$$

Now the magnitude of the transverse momenta of the outgoing charm and anticharm quark are almost equal. In the back-to-back D-meson and jet production, the total transverse momentum, $\boldsymbol{q}_T$, of the system is much smaller than the individual transverse momentum of the outgoing particles $\boldsymbol{K}_\perp$; i.e., $|\boldsymbol{q}_T| \ll |\boldsymbol{K}_\perp|$. Using Eq. (17), we get

$$d^2\boldsymbol{P}_{hT}d^2\boldsymbol{p}_{2\perp} = z d^2\boldsymbol{q}_T d^2\boldsymbol{K}_\perp. \quad (18)$$

In Eq. (12), the leptonic tensor $L^{\mu\nu}$ has the standard form

$$L^{\mu\nu} = e^2Q^2\left(-g^{\mu\nu} + \frac{2}{Q^2}(l^\mu l'^\nu + l^\nu l'^\mu)\right) = e^2Q^2\left(-g^{\mu\nu} + \frac{2}{Q^2}(2l^\mu l^\nu - l^\mu q^\nu - l^\nu q^\mu)\right), \quad (19)$$

where e is the electronic charge, and we average over the spins of the initial lepton. The four-momentum of the final scattered lepton is $l' = l - q$. By using Eq. (3), the leptonic tensor can be recast in the following form:

$$L^{\mu\nu} = e^2\frac{Q^2}{y^2}\Big[-(1+(1-y)^2)g_T^{\mu\nu} + 4(1-y)\epsilon_L^\mu\epsilon_L^\nu + 4(1-y)\left(\hat{l}_\perp^\mu\hat{l}_\perp^\nu + \frac{1}{2}g_T^{\mu\nu}\right) + 2(2-y)\sqrt{1-y}(\epsilon_L^\mu\hat{l}_\perp^\nu + \epsilon_L^\nu\hat{l}_\perp^\mu)\Big], \quad (20)$$

where the transverse metric tensor is defined as $g_T^{\mu\nu} = g^{\mu\nu} - n_+^\mu n_-^\nu - n_+^\nu n_-^\mu$, and the lightlike vectors can be written as below using Eq. (3)

$$n_-^\mu = P^\mu, \qquad n_+^\mu = \frac{1}{P\cdot q}(q^\mu + x_B P^\mu). \quad (21)$$

The longitudinal polarization vector of the virtual photon is given as

$$\epsilon_L^\mu(q) = \frac{1}{Q}\left(q^\mu + \frac{Q^2}{P\cdot q}P^\mu\right), \quad (22)$$

with $\epsilon_L^2(q) = 1$ and $\epsilon_L^\mu(q)q_\mu = 0$. The factor H in Eq. (12) contains the scattering amplitude of $\gamma^*(q) + g(k) \to c + \bar{c}$

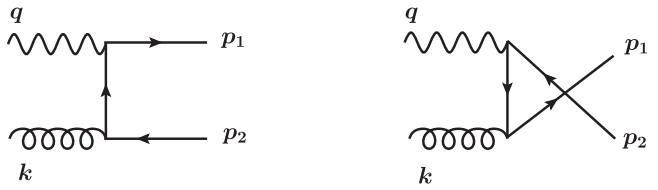

FIG. 1. Feynman diagrams for partonic subprocess $\gamma^*(q) + g(k) \to c(p_1) + \bar{c}(p_2)$ at LO.

partonic process; the corresponding Feynman diagrams are shown in Fig. 1.

In Eq. (12), the gluon correlator $\Phi_g^{\mu\nu}$, is a nonperturbative quantity that contains the dynamics of gluons inside a proton. At leading twist, for an unpolarized proton, the gluon correlator parametrized in terms of two gluon TMDs as [13]

$$\Phi_U^{\mu\nu}(x,\boldsymbol{k}_{\perp g}) = \frac{1}{2x}\left\{-g_T^{\mu\nu} f_1^g(x,\boldsymbol{k}_{\perp g}^2) + \left(\frac{k_{\perp g}^{\mu} k_{\perp g}^{\nu}}{M_p^2} + g_T^{\mu\nu}\frac{\boldsymbol{k}_{\perp g}^2}{2M_p^2}\right) \times h_1^{\perp g}(x,\boldsymbol{k}_{\perp g}^2)\right\}, \tag{23}$$

where f_1^g and $h_1^{\perp g}$, T-even TMDs encode the distribution of unpolarized and linearly polarized gluons for a given collinear momentum fraction x and the transverse momentum $k_{\perp g}$, respectively. These TMDs can be nonzero even if initial and final state interactions are absent in the process. Similarly, for the transversely polarized proton [13], we have

$$\Phi_T^{\mu\nu}(x,\boldsymbol{k}_{\perp g}) = \frac{1}{2x}\left\{-g_T^{\mu\nu}\frac{\epsilon_T^{\rho\sigma} k_{\perp g\rho} S_{T\sigma}}{M_p} f_{1T}^{\perp g}(x,\boldsymbol{k}_{\perp g}^2) + i\epsilon_T^{\mu\nu}\frac{k_{\perp g}\cdot S_T}{M_p} g_{1T}^g(x,\boldsymbol{k}_{\perp g}^2) + \frac{k_{\perp g\rho}\epsilon_T^{\rho\{\mu} k_{\perp g}^{\nu\}}}{2M_p^2}\frac{k_{\perp g}\cdot S_T}{M_p} h_{1T}^{\perp g}(x,\boldsymbol{k}_{\perp g}^2) - \frac{k_{\perp g\rho}\epsilon_T^{\rho\{\mu} S_T^{\nu\}} + S_{T\rho}\epsilon_T^{\rho\{\mu} k_{\perp g}^{\nu\}}}{4M_p} h_{1T}^{g}(x,\boldsymbol{k}_{\perp g}^2)\right\}, \tag{24}$$

where the notations are the antisymmetric tensor $\epsilon_T^{\mu\nu} = \epsilon^{\mu\nu\rho\sigma} P_\rho n_{+\sigma}$ with $\epsilon_T^{12} = +1$, and the symmetrization tensor $p_{T\rho}\epsilon_T^{\rho\{\mu} p_T^{\nu\}} = p_{T\rho}(\epsilon_T^{\rho\mu} p_T^{\nu} + \epsilon_T^{\rho\nu} p_T^{\mu})$. In Eq. (24), we have three T-odd TMDs: The Sivers function, $f_{1T}^{\perp g}$, describes the density of unpolarized gluons, while $h_{1T}^{\perp g}$ and h_{1T}^{g} are linearly polarized gluon densities of a transversely polarized proton. The T-even TMD, g_{1T}^g, is the distribution of circularly polarized gluons in a transversely polarized proton, which does not contribute here since it is in the antisymmetric part of the correlator.

After performing the integration over z_2, x, and $\boldsymbol{k}_{\perp g}$ in Eq. (12), we get

$$\frac{\mathrm{d}\sigma^{ep\to e+D+\bar{c}+X}}{\mathrm{d}Q^2\mathrm{d}y\mathrm{d}z_h\mathrm{d}^2\boldsymbol{q}_T\mathrm{d}^2\boldsymbol{K}_\perp} = \frac{1}{ys^2}\frac{1}{16(2\pi)^4}\int \mathrm{d}z\, D(z) \times \frac{1}{Q^4} L^{\mu\nu}(l,q)\Phi_g^{\rho\sigma}(x,\boldsymbol{q}_T) H_{\mu\rho}^{\gamma^* g\to c\bar{c}} \times H_{\nu\sigma}^{*\gamma^* g\to c\bar{c}} \frac{zJ(z)}{z_h(1-z_1)}. \tag{25}$$

IV. AZIMUTHAL ASYMMETRIES

In the kinematics wherein the D meson and the jet are back-to-back in the transverse plane (as discussed above), we can write the cross section as the sum of unpolarized and transversely polarized cross sections as [33],

$$\frac{\mathrm{d}\sigma}{\mathrm{d}Q^2\mathrm{d}y\mathrm{d}z_h\mathrm{d}^2\boldsymbol{q}_T\mathrm{d}^2\boldsymbol{K}_\perp} \equiv \mathrm{d}\sigma(\phi_S,\phi_T) = \mathrm{d}\sigma^U(\phi_T,\phi_\perp) + \mathrm{d}\sigma^T(\phi_S,\phi_T). \tag{26}$$

The cross section for the unpolarized proton is written as the linear sum of $\cos\phi_T$ and $\cos\phi_\perp$ harmonics convoluted with the fragmentation function,

$$\mathrm{d}\sigma^U = \mathcal{N}\int \mathrm{d}z\Big[(\mathcal{A}_0 + \mathcal{A}_1\cos\phi_\perp + \mathcal{A}_2\cos 2\phi_\perp) f_1^g(x,\boldsymbol{q}_T^2) + (\mathcal{B}_0\cos 2\phi_T + \mathcal{B}_1\cos(2\phi_T - \phi_\perp) + \mathcal{B}_2\cos 2(\phi_T - \phi_\perp) + \mathcal{B}_3\cos(2\phi_T - 3\phi_\perp) + \mathcal{B}_4\cos(2\phi_T - 4\phi_\perp))\frac{\boldsymbol{q}_T^2}{M_p^2} h_1^{\perp g}(x,\boldsymbol{q}_T^2)\Big] D(z), \tag{27}$$

where $\mathcal{N}$ is the normalization factor given as

$$\mathcal{N} = \frac{\alpha^2\alpha_s e_c^2}{\pi y^3 s^2 x}. \tag{28}$$

The coefficients mentioned in the above equation are the result of the contribution from different helicities of the virtual photon and the linearly polarized gluon. For instance, if the azimuthal angle of the final scattered lepton is not measured, then only one modulation term in Eq. (27) is defined, and the cross section is expressed as

$$d\sigma^U = \mathcal{N}\int dz\left[\mathcal{A}_0 f_1^g(x,\boldsymbol{q}_T^2) + \mathcal{B}_2\cos 2(\phi_T-\phi_\perp)\frac{\boldsymbol{q}_T^2}{M_p^2}h_1^{\perp g}(x,\boldsymbol{q}_T^2)\right]D(z), \tag{29}$$

while in the case of a transversely polarized proton,

$$\begin{aligned} d\sigma^T = \mathcal{N}|\boldsymbol{S}_T|\int dz\Big[&\sin(\phi_S-\phi_T)(\mathcal{A}_0+\mathcal{A}_1\cos\phi_\perp+\mathcal{A}_2\cos 2\phi_\perp)\frac{|\boldsymbol{q}_T|}{M_p}f_{1T}^{\perp g}(x,\boldsymbol{q}_T^2)+\cos(\phi_S-\phi_T)\\ &\times(\mathcal{B}_0\sin 2\phi_T+\mathcal{B}_1\sin(2\phi_T-\phi_\perp)+\mathcal{B}_2\sin 2(\phi_T-\phi_\perp)+\mathcal{B}_3\sin(2\phi_T-3\phi_\perp)+\mathcal{B}_4\sin(2\phi_T-4\phi_\perp))\\ &\times\frac{|\boldsymbol{q}_T|^3}{M_p^3}h_{1T}^{\perp g}(x,\boldsymbol{q}_T^2)+(\mathcal{B}_0\sin(\phi_S+\phi_T)+\mathcal{B}_1\sin(\phi_S+\phi_T-\phi_\perp)+\mathcal{B}_2\sin(\phi_S+\phi_T-2\phi_\perp)\\ &+\mathcal{B}_3\sin(\phi_S+\phi_T-3\phi_\perp)+\mathcal{B}_4\sin(\phi_S+\phi_T-4\phi_\perp))\frac{|\boldsymbol{q}_T|}{M_p}h_{1T}^{g}(x,\boldsymbol{q}_T^2)\Big]D(z), \end{aligned} \tag{30}$$

where ϕ_S, ϕ_T, and $\phi_\perp$ are the azimuthal angles of the three-vectors $\boldsymbol{S}_T$, $\boldsymbol{q}_T$, and $\boldsymbol{K}_\perp$, respectively, measured with respect to the lepton plane ($\phi_\ell = \phi_{\ell'} = 0$) as shown in Fig. 2. The coefficients of the different angular modulations $\mathcal{A}_i$ with $i = 0, 1, 2$ and $\mathcal{B}_j$ with $j = 0, 1, 2, 3, 4$ are given in the Appendix.

The weighted azimuthal asymmetry gives the ratio of the specific gluon TMD over unpolarized f_1^g and is defined as [36]

$$A^{W(\phi_S,\phi_T)} \equiv 2\frac{\int d\phi_S d\phi_T d\phi_\perp W(\phi_S,\phi_T)d\sigma(\phi_S,\phi_T,\phi_\perp)}{\int d\phi_S d\phi_T d\phi_\perp d\sigma(\phi_S,\phi_T,\phi_\perp)}, \tag{31}$$

where the denominator is given by

$$\begin{aligned} &\int d\phi_S d\phi_T d\phi_\perp d\sigma(\phi_S,\phi_T,\phi_\perp)\\ &\quad=\int d\phi_S d\phi_T d\phi_\perp d\sigma^U(\phi_T,\phi_\perp)\\ &\quad=(2\pi)^3\mathcal{N}\int dz\mathcal{A}_0 f_1^g(x,\boldsymbol{q}_T^2)D(z). \end{aligned} \tag{32}$$

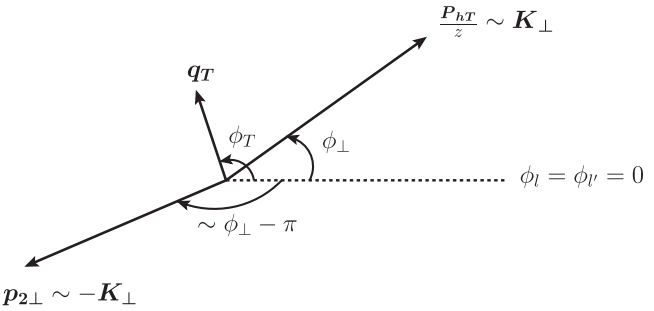

FIG. 2. Representation of the azimuthal angles in the production of D meson and jet in SIDIS process.

By integrating over the azimuthal angle $\phi_\perp$, the transversely polarized cross section, Eq. (30), can be simplified further as

$$\begin{aligned} \int d\phi_\perp d\sigma^T = 2\pi|\boldsymbol{S}_T|\frac{|\boldsymbol{q}_T|}{M_p}\int dz\Big[&\mathcal{A}_0\sin(\phi_S-\phi_T)f_{1T}^{\perp g}(x,\boldsymbol{q}_T^2)\\ &-\frac{1}{2}\mathcal{B}_0\sin(\phi_S-3\phi_T)\frac{|\boldsymbol{q}_T|^2}{M_p^2}h_{1T}^{\perp g}(x,\boldsymbol{q}_T^2)\\ &+\mathcal{B}_0\sin(\phi_S+\phi_T)h_1^g(x,\boldsymbol{q}_T^2)\Big]D(z), \end{aligned} \tag{33}$$

where we have used the relation

$$h_1^g \equiv h_{1T}^g + \frac{\boldsymbol{p}_T^2}{2M_p^2}h_{1T}^{\perp g}, \tag{34}$$

where h_1^g (T-odd) is the helicity flip gluon distribution, which is chiral-even and vanishes upon integration of transverse momentum [52]. In contrast, the quark distribution is chiral-odd (T-even) and survives even after the transverse momentum integration. The $h_1^{\perp g}$ gluon TMD could be extracted by studying the following two azimuthal asymmetries,

$$A^{\cos 2\phi_T} = \frac{\boldsymbol{q}_T^2}{M_p^2}\frac{\int dz\mathcal{B}_0 D(z)h_1^{\perp g}(x,\boldsymbol{q}_T^2)}{\int dz\mathcal{A}_0 D(z)f_1^g(x,\boldsymbol{q}_T^2)}, \tag{35}$$

and

$$A^{\cos 2(\phi_T-\phi_\perp)} = \frac{\boldsymbol{q}_T^2}{M_p^2}\frac{\int dz\mathcal{B}_2 D(z)h_1^{\perp g}(x,\boldsymbol{q}_T^2)}{\int dz\mathcal{A}_0 D(z)f_1^g(x,\boldsymbol{q}_T^2)}. \tag{36}$$

Using Eq. (33) with $|\boldsymbol{S}_T| = 1$, one could utilize the following asymmetries to extract the $f_{1T}^{\perp g}$, h_1^g, and $h_{1T}^{\perp g}$ TMDs,

$$A^{\sin(\phi_S-\phi_T)} = \frac{|\boldsymbol{q}_T|}{M_p}\frac{\int \mathrm{d}z\, \mathcal{A}_0 D(z) f_{1T}^{\perp g}(x,\boldsymbol{q}_T^2)}{\int \mathrm{d}z\, \mathcal{A}_0 D(z) f_1^g(x,\boldsymbol{q}_T^2)}, \tag{37}$$

$$A^{\sin(\phi_S+\phi_T)} = \frac{|\boldsymbol{q}_T|}{M_p}\frac{\int \mathrm{d}z\, \mathcal{B}_0 D(z) h_1^g(x,\boldsymbol{q}_T^2)}{\int \mathrm{d}z\, \mathcal{A}_0 D(z) f_1^g(x,\boldsymbol{q}_T^2)}, \tag{38}$$

and

$$A^{\sin(\phi_S-3\phi_T)} = -\frac{|\boldsymbol{q}_T|^3}{2M_p^3}\frac{\int \mathrm{d}z\, \mathcal{B}_0 D(z) h_{1T}^{\perp g}(x,\boldsymbol{q}_T^2)}{\int \mathrm{d}z\, \mathcal{A}_0 D(z) f_1^g(x,\boldsymbol{q}_T^2)}. \tag{39}$$

A. Positivity bounds

The upper limit of the azimuthal asymmetries as defined above can be reached when the polarized gluon TMDs saturate the positivity bounds that are independent of any specific model [13,53].

$$\begin{aligned}
\frac{|\boldsymbol{q}_T|}{M_p}|f_{1T}^{\perp g}(x,\boldsymbol{q}_T^2)| &\le f_1^g(x,\boldsymbol{q}_T^2),\\
\frac{\boldsymbol{q}_T^2}{2M_p^2}|h_1^{\perp g}(x,\boldsymbol{q}_T^2)| &\le f_1^g(x,\boldsymbol{q}_T^2),\\
\frac{|\boldsymbol{q}_T|}{M_p}|h_1^g(x,\boldsymbol{q}_T^2)| &\le f_1^g(x,\boldsymbol{q}_T^2),\\
\frac{|\boldsymbol{q}_T|^3}{2M_p^3}|h_{1T}^{\perp g}(x,\boldsymbol{q}_T^2)| &\le f_1^g(x,\boldsymbol{q}_T^2).
\end{aligned} \tag{40}$$

Using the positivity bounds on the gluon TMDs given in Eqs. (35)–(39) and for the fixed kinematical variables, we obtain the following upper bounds on the absolute value of the $A^{\cos 2\phi_T}$ and $A^{\cos 2(\phi_T-\phi_\perp)}$ asymmetries,

$$|A^{\cos 2\phi_T}| \le 2\frac{|\mathcal{B}_0|}{\mathcal{A}_0}, \qquad |A^{\cos 2(\phi_T-\phi_\perp)}| \le 2\frac{|\mathcal{B}_2|}{\mathcal{A}_0}, \tag{41}$$

and the upper bound for the Sivers asymmetry, $A^{\sin(\phi_S-\phi_T)}$, becomes equal to one, while the upper bounds for the other asymmetries can be determined using their relations with other asymmetries, such as

$$\begin{aligned}
|A^{\sin(\phi_S+\phi_T)}| &= \frac{1}{2}|A^{\cos 2\phi_T}|,\\
|A^{\sin(\phi_S-3\phi_T)}| &= \frac{1}{2}|A^{\cos 2(\phi_T-\phi_\perp)}|.
\end{aligned} \tag{42}$$

B. Gaussian parametrization of TMDs

The numerical estimate of the asymmetries depends on the parametrization used for the TMDs. In this work, we estimate the asymmetries using Gaussian parametrization. For the unpolarized gluon TMD, we adopt a parametrization given by

$$f_1^g(x,\boldsymbol{q}_T^2) = f_1^g(x,\mu)\frac{e^{-\boldsymbol{q}_T^2/\langle q_T^2\rangle}}{\pi\langle q_T^2\rangle}, \tag{43}$$

where $f_1^g(x,\mu)$ is the collinear gluon PDF at the probing scale $\mu = \sqrt{m_h^2+Q^2}$ [54]. We use MSTW2008 set [55] for the collinear PDF. The Gaussian parametrization of TMDs with a Gaussian width $\langle q_T^2\rangle = 1\ \mathrm{GeV}^2$ for gluons [49]. We adopt the following Gaussian parametrization for the linearly polarized gluon TMD $h_1^{\perp g}$ as given in Refs. [56,57],

$$h_1^{\perp g}(x,\boldsymbol{q}_T^2) = \frac{M_p^2 f_1^g(x,\mu)}{\pi\langle q_T^2\rangle^2}\frac{2(1-r)}{r}e^{1-\frac{\boldsymbol{q}_T^2}{r\langle q_T^2\rangle}}, \tag{44}$$

where M_p is the proton mass, r (with $0<r<1$), and the average intrinsic transverse momentum width of the incoming gluon, $\langle q_T^2\rangle$, are parameters of this model. In our numerical estimation, we take $r=1/3$ and $\langle q_T^2\rangle = 1\ \mathrm{GeV}^2$.

Similarly, for the gluon Sivers function (GSF) $f_{1T}^{\perp g}$, we have used the parametrization given in Refs. [30,58,59],

$$\begin{aligned}
\Delta^N f_{g/p^\uparrow}(x,q_T) &= \left(-\frac{2|\boldsymbol{q}_T|}{M_P}\right) f_{1T}^{\perp g}(x,q_T)\\
&= 2\frac{\sqrt{2e}}{\pi}\mathcal{N}_g(x) f_{g/p}(x)\sqrt{\frac{1-\rho}{\rho}}q_T\frac{e^{-\boldsymbol{q}_T^2/\rho\langle q_T^2\rangle}}{\langle q_T^2\rangle^{3/2}},
\end{aligned} \tag{45}$$

with $0<\rho<1$. The x dependence of the gluon Sivers function is encoded in the $\mathcal{N}_g(x)$, and it is generally written as

$$\mathcal{N}_g(x) = N_g x^\alpha (1-x)^\beta \frac{(\alpha+\beta)^{(\alpha+\beta)}}{\alpha^\alpha \beta^\beta}. \tag{46}$$

The parameters N_g, α, and β are determined from global fits to experimental data on SSAs in inclusive hadron production processes [30], while the extracted best-fit parameters at $\langle q_T^2\rangle = 1\ \mathrm{GeV}^2$ are

$$N_g = 0.25, \qquad \alpha = 0.6, \qquad \beta = 0.6, \qquad \rho = 0.1. \tag{47}$$

C. Fragmentation function of the D meson

At leading order (LO), the charm quark produced in the virtual photon-gluon fusion process fragments to form the D meson in the final state. In our kinematics, we can consider the D meson to be collinear to the fragmenting heavy quark. This means that the transverse momentum of the D meson is related to the charm quark's transverse momentum through Eq. (9). The LO fragmentation function for the $c \to D^0$ process is parametrized as

$$D(z,\mu_0) = \frac{Nz(1-z)^2}{[(1-z)^2+\epsilon z]^2} \tag{48}$$

which is given by [54]. The parameters are $N = 0.694$, $\epsilon = 0.101$, and are fitted using OPAL Collaboration data at CERN LEP-I at the $\mu_0 = m_c = 1.5$ GeV. The scale evolution of the collinear fragmentation function is given by the DGLAP equation. Here, we ignore the scale evolution of the fragmentation function. A similar approach is followed in [46–49].

V. RESULTS AND DISCUSSIONS

A. Unpolarized cross section

In this section, we present numerical results for the unpolarized cross section of D-meson and jet production in the SIDIS process. The LO contribution comes only from the gluon-initiated partonic subprocess, i.e., $\gamma^* + g \to c + \bar{c} \to D + \bar{c}$, whereas the contribution from the quark-initiated process occurs at NLO. After integrating over the azimuthal angles, only the $\mathcal{A}_0$ term contributes to the unpolarized cross section given in Eq. (27), and its expression is given in Appendix. We used the Gaussian parametrization, given in Eq. (43) for the unpolarized transverse momentum dependent (TMD) gluon distribution function $f_1^g(x, \boldsymbol{q}_T^2)$. We consider the situation, in which the produced D meson and jet are almost back to back, with $q_T^2 \ll Q^2$ and $|\boldsymbol{q}_T| \ll |\boldsymbol{K}_\perp|$, which allows us to assume the TMD factorization for the cross section. We estimate the cross section at the cm energy of the EIC with $\sqrt{s} = 140$ and 45 GeV, and we choose the following kinematical constraints. The range of integration of the virtuality of the photon (Q^2) is $3 < Q^2 < 100$ GeV^2, the momentum fraction z carried by the D meson from the charm quark, is in the range $0 < z < 1$. The inelasticity variable y is fixed from the definition of the invariant mass of photon-proton system, denoted as $W_{\gamma p}$, and it is in the range $20 < W_{\gamma p} < 80$ GeV for $\sqrt{s} = 140$ GeV, and $10 < W_{\gamma p} < 40$ GeV for $\sqrt{s} = 45$ GeV. In this kinematics, q_T is the sum of the transverse momenta of the outgoing charm and anticharm quarks, which is equal to the transverse momentum of the initial gluon, q_T varies in the range $0 < q_T < 1$ GeV. The transverse momentum of the outgoing particles, i.e., the D meson, and the jet, denoted as $K_\perp$, is considered to be greater than 2 GeV. This condition, $|\boldsymbol{q}_T| \ll |\boldsymbol{K}_\perp|$, implies that the D meson and jet are produced almost back to back in the process. We have set the upper and lower bounds on the momentum fraction of the hadron as $0.1 < z_h < 0.9$. To avoid the unphysical contribution from the endpoints of the z_h, we imposed the aforementioned kinematic restriction on the z_h.

In Fig. 3, the unpolarized differential cross section is shown as a function of the transverse momentum, $K_\perp$, of the D meson and z_h, the momentum fraction carried by the D meson from the virtual photon. The blue dashed line represents the cross section for $\sqrt{s} = 140$ GeV, while the red dash-dotted line represents the cross section for $\sqrt{s} = 45$ GeV. The cross section is larger for higher cm energy due to the low momentum fraction x region being probed at higher cm energy compared to lower cm energy, and the density of gluons is higher in low x region. In the left panel of Fig. 3, the cross section falls rapidly with increasing $K_\perp$ for lower cm energy, which is expected, as the production of high transverse momentum particles

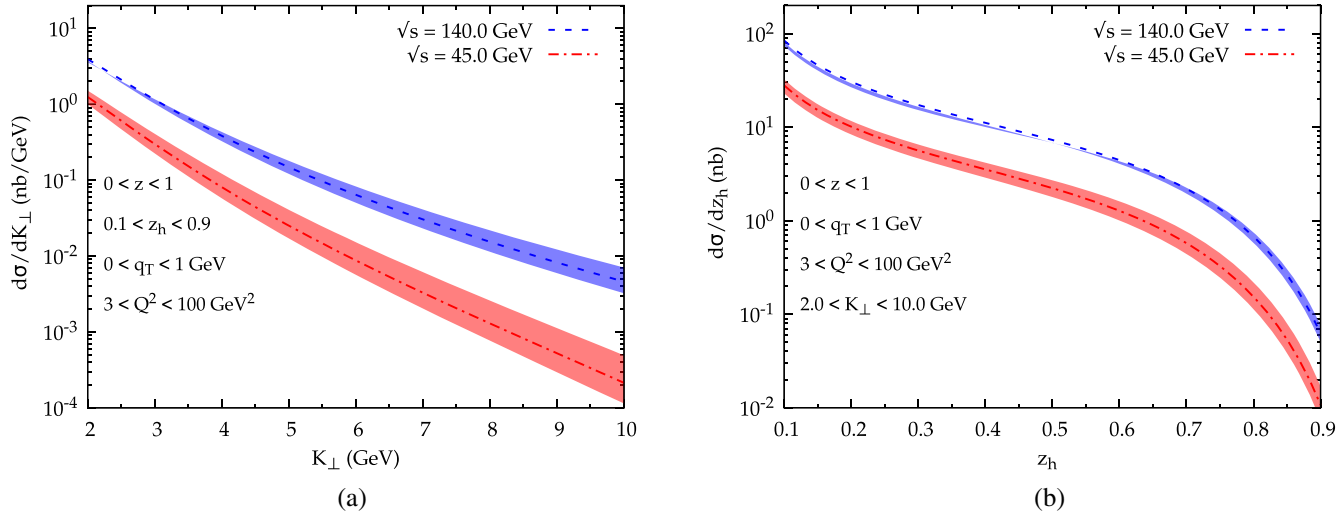

FIG. 3. Unpolarized differential scattering cross section of $e + p \to e + D + \text{jet} + X$ process as a function of $K_\perp$ (left) and z_h (right). For $K_\perp$ and z_h variations, the z, Q^2, and q_T are integrated over the regions $0 < z < 1$, $3 < Q^2 < 100$ GeV^2 and $0.0 < q_T < 1.0$ GeV. For $\sqrt{s} = 140$ GeV, the range of $W_{\gamma p}$ is $20 < W_{\gamma p} < 80$ GeV, while for $\sqrt{s} = 45$ GeV, the range is $10 < W_{\gamma p} < 40$ GeV. For $K_\perp$ variation, we have taken $0.1 < z_h < 0.9$, and for z_h variation, $2.0 < K_\perp < 10.0$ GeV. The bands are obtained by varying the factorization scale in the range $\frac{1}{2}\mu < \mu < 2\mu$.

becomes less probable at lower energies. In the right panel of Fig. 3, the scattering cross section is plotted as a function of z_h, which is obtained by integrating $K_\perp$ over the range $2 < K_\perp < 10$ GeV. It is observed that the cross section decreases as z_h increases. In Fig. 3, the band represents the theoretical uncertainty, which is obtained by varying the factorization scale $\mu = \sqrt{Q^2 + m_h^2}$ from 0.5μ to 2μ. The width of the uncertainty band in Fig. 3 for $K_\perp$ variation becomes wider at high $K_\perp$, while it is narrow at small $K_\perp$. The scale uncertainty is expected to decrease at higher order in QCD.

B. Upper bounds

In this section, we present the numerical estimates of the upper bounds for $\cos 2\phi_T$ and $\cos 2(\phi_T - \phi_\perp)$ asymmetries by saturating the positivity relations of the TMDs. In Figs. 4–6, we have plotted the upper bounds for the azimuthal asymmetries $\cos 2\phi_T$ (left panel) and $\cos 2(\phi_T - \phi_\perp)$ (right panel) in the process $e + p \to e + D + \text{jet} + X$. The upper bound of the asymmetries depends on $\sqrt{s}$; with other kinematical variables fixed, we observed that the upper bound is about 3–4% higher for $\sqrt{s} = 45$ GeV compared to $\sqrt{s} = 140$ GeV. In the plot, we show the upper bound for $\sqrt{s} = 45$ GeV. We plotted the upper bound as a function of the transverse momentum, $K_\perp$, momentum fraction, z_h and rapidity, y at two different virtualities of the photon $Q^2 = 10, 20$ GeV^2. We integrated the variables z and q_T variables within the range 0 to 1. The variation of $K_\perp$ is shown in Fig. 4 for fixed values of z_h and y, the variation of z_h is shown in Fig. 5 for the fixed values of $K_\perp$ and y, and the y variation is shown in Fig. 6 for the fixed values of $K_\perp$ and z_h.

From Figs. 4–6, it can be observed that the upper bound of $\cos 2\phi_T$ azimuthal asymmetry increases with increasing virtuality of the photon (Q^2). In Fig. 4, one can see that for a given Q^2 the magnitude of the upper bound of $\cos 2\phi_T$ azimuthal asymmetry decreases with increasing $K_\perp$. This can be attributed to the increase in the longitudinal momentum fraction of the initial gluon x as $K_\perp$ increases, which leads to the vanishing of the gluon PDF as x approaches 1. The behavior of $K_\perp$ variation of the upper bound of $\cos 2(\phi_T - \phi_\perp)$ azimuthal asymmetry for two different resolutions of the photon exhibits a somewhat different behavior; in the small $K_\perp$ region, the high virtuality asymmetry dominates, while at high $K_\perp$, the low virtuality curve dominates. With increasing $K_\perp$, the $\cos 2(\phi_T - \phi_\perp)$ azimuthal asymmetry initially increases, reaches a peak at around 2.5 GeV for $Q^2 = 10$ GeV^2 and 3 GeV for $Q^2 = 20$ GeV^2, and then decreases. Qualitatively, $\cos 2\phi_T$ azimuthal asymmetry decreases as $K_\perp$ increases.

Figure 5 shows the z_h variation for two different virtualities of the photon of the upper bound of the $\cos 2\phi_T$ (left panel) and $\cos 2(\phi_T - \phi_\perp)$ (right panel) azimuthal asymmetries. The upper bounds increase as the virtuality of the photon increases, and both azimuthal asymmetries show a maximum at $z_h \approx 0.3$. The upper bound of $\cos 2(\phi_T - \phi_\perp)$ azimuthal asymmetry becomes zero and then changes sign at higher values of z_h. This is due to a change in the sign of the coefficient $\mathcal{B}_1$ in the numerator. In Fig. 6, the upper bounds for $\cos 2\phi_T$ (left panel) and $\cos 2(\phi_T - \phi_\perp)$ (right panel) are plotted as a function of y. As y increases, the magnitude of $\cos 2\phi_T$ azimuthal asymmetry decreases and reaches its minimum at $y = 1$ due to the vanishing of the coefficient $\mathcal{B}_0$ at $y = 1$.

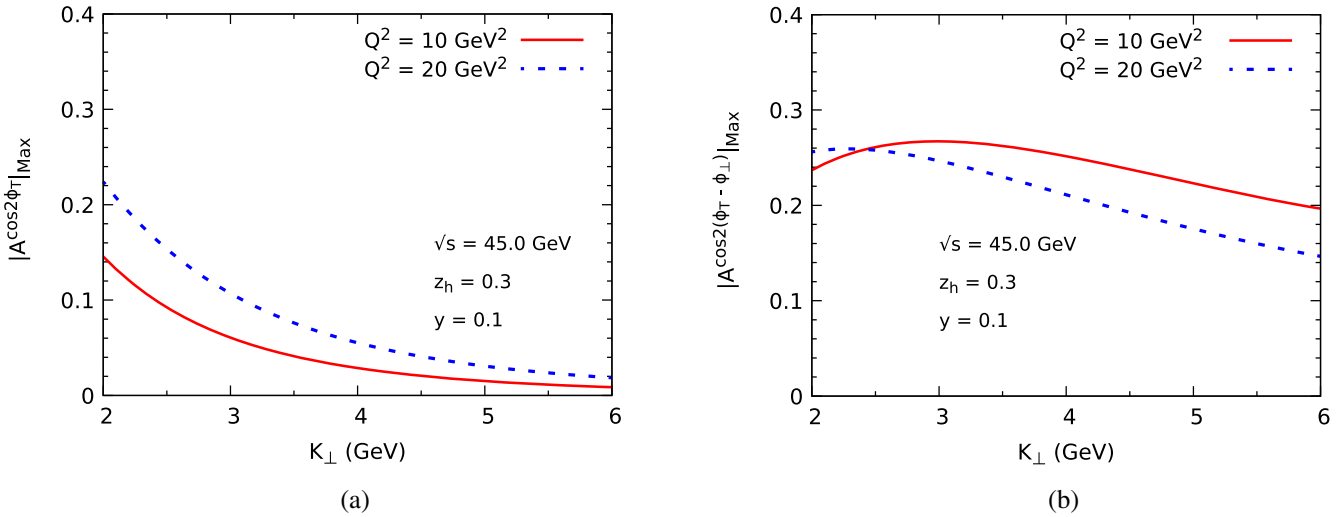

FIG. 4. Upper bound for the $A^{\cos 2\phi_T}$ (left panel) and $A^{\cos 2(\phi_T - \phi_\perp)}$ (right panel) azimuthal asymmetries in the $e + p \to e + D + \text{jet} + X$ process as a function of $K_\perp$ at EIC $\sqrt{s} = 45$ GeV for fixed values of $y = 0.1$, $z_h = 0.3$, and $Q^2 = 10, 20$ GeV^2. The kinematical variables z and q_T are integrated from [0,1].

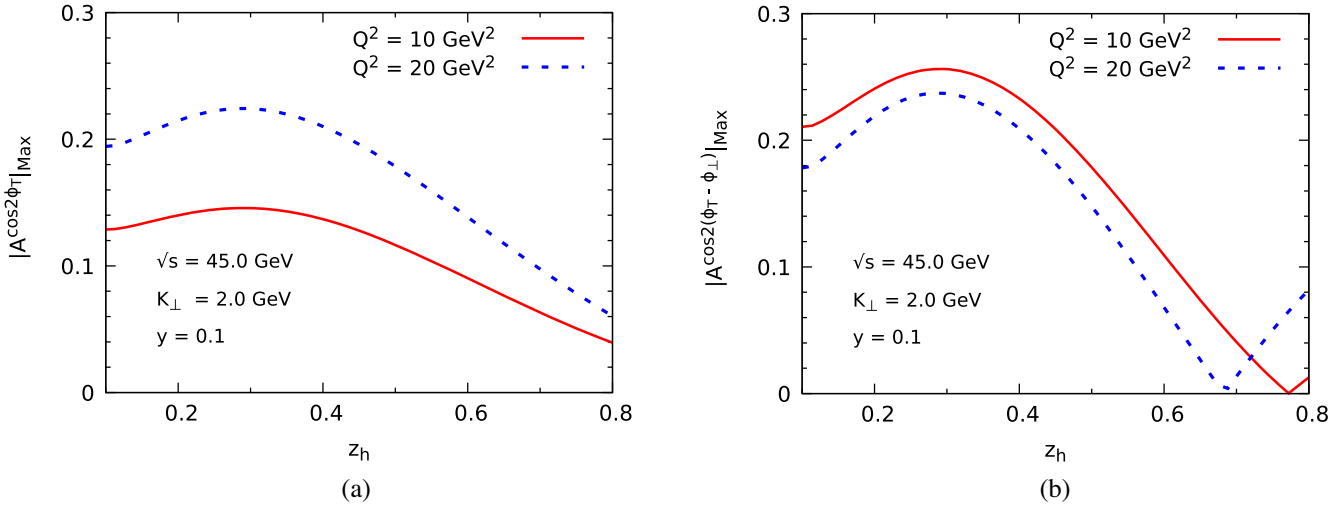

FIG. 5. Upper bound for the $A^{\cos 2\phi_T}$ (left panel) and $A^{\cos 2(\phi_T-\phi_\perp)}$ (right panel) azimuthal asymmetries in the $e+p\to e+D+\text{jet}+X$ process as a function of z_h at EIC $\sqrt{s}=45$ GeV for fixed values of $y=0.1$, $K_\perp=2$ GeV, and $Q^2=10$, 20 GeV^2. The kinematical variables z and q_T are integrated from [0,1].

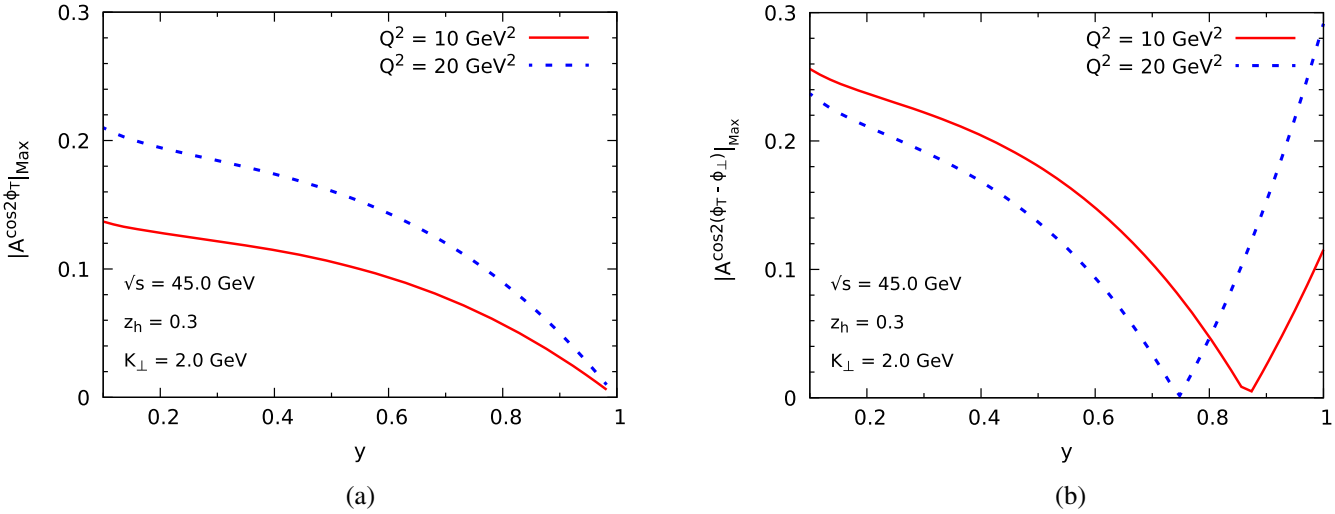

FIG. 6. Upper bound for the $A^{\cos 2\phi_T}$ (left panel) and $A^{\cos 2(\phi_T-\phi_\perp)}$ (right panel) azimuthal asymmetries in the $e+p\to e+D+\text{jet}+X$ process as a function of y at EIC $\sqrt{s}=45$ GeV for fixed values of $z_h=0.3$, $K_\perp=2$ GeV, and $Q^2=10$, 20 GeV^2. The kinematical variables z and q_T are integrated from [0,1].

For $\cos 2(\phi_T-\phi_\perp)$, the coefficient $\mathcal{B}_2$ contributes, which involves both longitudinal and transverse polarization of the photon. At $y=1$, only the contribution from transverse photons leads to a larger asymmetry. The magnitude of $\cos 2\phi_T$ azimuthal asymmetry increases as the virtuality of the photon increases from $Q^2=10\,\text{GeV}^2$ to $Q^2=20\,\text{GeV}^2$. In contrast, the magnitude of the upper bound of $\cos 2(\phi_T-\phi_\perp)$ is larger for $Q^2=10$ GeV^2 compared to $Q^2=20$ GeV^2 for low values of y. The upper bound of $\cos 2(\phi_T-\phi_\perp)$ azimuthal asymmetry becomes zero and then changes sign because the numerator switches the sign from positive to negative. The value of y where this happens depends on the photon virtuality.

C. Gaussian parametrization

In this section, we present the numerical results obtained by parameterizing the gluon TMDs using the Gaussian parametrization provided in Eqs. (43) and (44). In Figs. 7–10, $\cos 2\phi_T$ (left panel) and $\cos 2(\phi_T-\phi_\perp)$ (right panel) azimuthal asymmetries are shown as functions of $K_\perp$, z_h, y, and q_T, respectively, at $\sqrt{s}=45$ GeV. In these plots, the kinematical variables are chosen to maximize the asymmetry. In Fig. 7, we compare the asymmetries for two different virtualities of the photon, Q^2. From Fig. 7, one can see that $\cos 2\phi_T$ asymmetry is higher for higher Q^2 value, but in the low $K_\perp$ region, $\cos 2(\phi_T-\phi_\perp)$ asymmetry is larger for lower value of Q^2. Moreover, the asymmetries

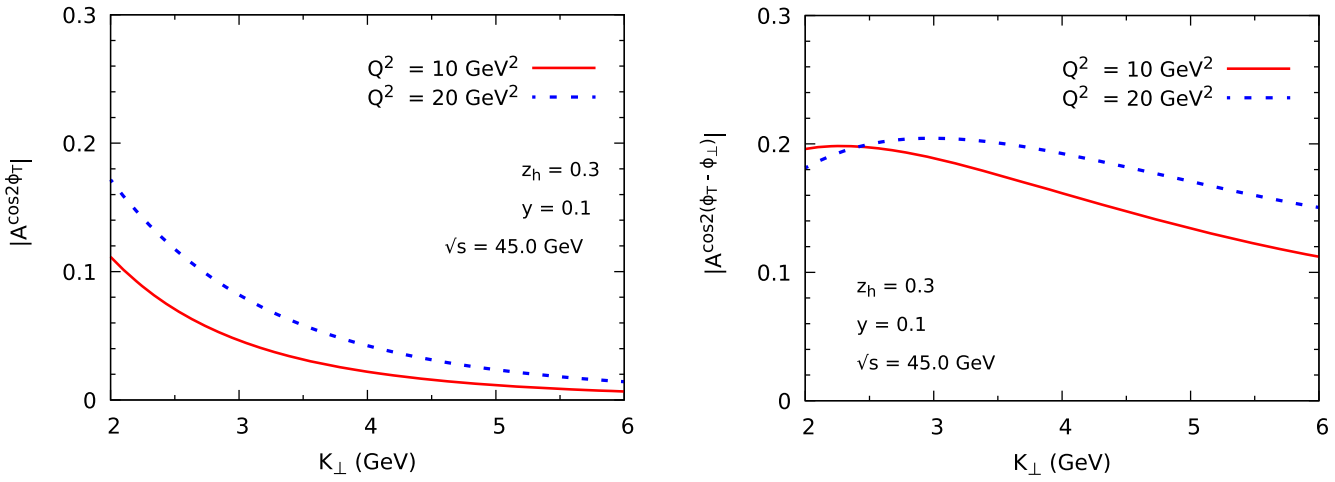

FIG. 7. Absolute values of $\cos 2\phi_T$ (left panel) and $\cos 2(\phi_T - \phi_\perp)$ (right panel) azimuthal asymmetries in the $e + p \to e + D +$ jet $+ X$ process as a function of $K_\perp$ for $\sqrt{s} = 45$ GeV at fixed values of $y = 0.1$, $z_h = 0.3$ for two values of $Q^2 = 10, 20$ GeV^2. The z and q_T are integrated over $0 < z < 1$, $0 < q_T < 1$ GeV.

decrease as $K_\perp$ increases. However, the $\cos 2\phi_T$ asymmetry decreases much faster compared to $\cos 2(\phi_T - \phi_\perp)$. The variation of both the azimuthal asymmetries as a function of z_h is shown in Fig. 8. For both Q^2 values, the azimuthal asymmetries are at a maximum at $z_h = 0.3$. As shown in $\cos 2\phi_T$ plot, the asymmetry initially increases with z_h, reaches a maximum value, and then decreases. In the $\cos 2(\phi_T - \phi_\perp)$ plot, the asymmetry increases first and reaches its maximum value. After that, it decreases to zero and then becomes negative with increasing z_h. This qualitative behavior depends on the relative dominance of the term with transverse polarization of photons [first term of Eq. (20)] and the term with longitudinal polarization [second term of Eq. (20)]. The magnitude of $\cos 2(\phi_T - \phi_\perp)$ vanishes at $z_h = 0.6$ for $Q^2 = 20$ GeV^2 and at $z_h = 0.7$ for $Q^2 = 10$ GeV^2. Unlike the $\cos 2\phi_T$ asymmetry, the $\cos 2(\phi_T - \phi_\perp)$ asymmetry is larger for a lower value of Q^2. The y variation of $\cos 2\phi_T$ and $\cos 2(\phi_T - \phi_\perp)$ azimuthal asymmetries is shown in Fig. 9. The $\cos 2\phi_T$ azimuthal asymmetry decreases monotonically as y increases. On the other hand, the $\cos 2(\phi_T - \phi_\perp)$ azimuthal asymmetry shows different behavior in the low and high y regions. In the low y region, the $\cos 2(\phi_T - \phi_\perp)$ azimuthal asymmetry shows a similar behavior to the $\cos 2\phi_T$ azimuthal asymmetry. As y increases, the asymmetry becomes zero ($y \approx 0.7$ for

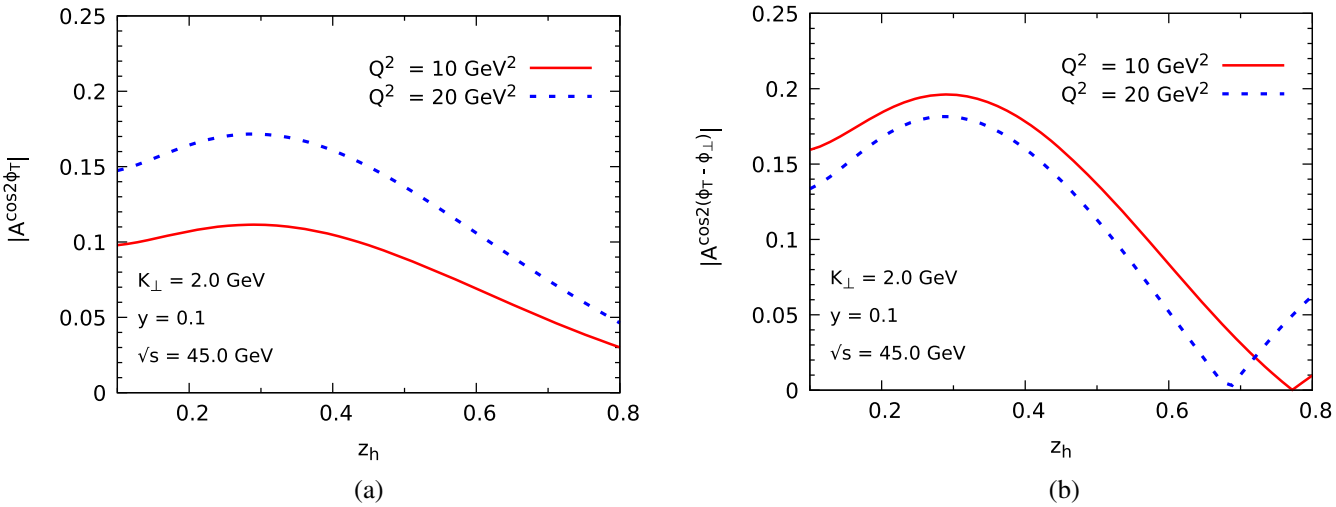

FIG. 8. Absolute values of $\cos 2\phi_T$ (left panel) and $\cos 2(\phi_T - \phi_\perp)$ (right panel) azimuthal asymmetries in the $e + p \to e + D +$ jet $+ X$ process as a function of z_h for $\sqrt{s} = 45$ GeV at fixed values of $y = 0.1$, $K_\perp = 2$ GeV for two values of $Q^2 = 10, 20$ GeV^2. The z and q_T are integrated over $0 < z < 1$, $0 < q_T < 1$ GeV.

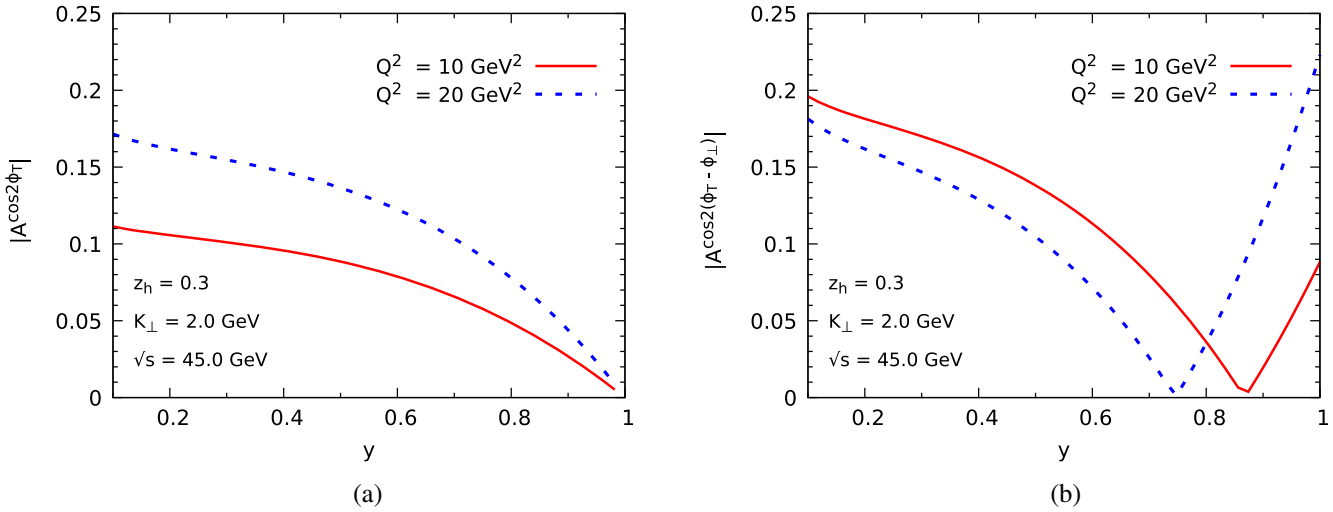

FIG. 9. Absolute values of $\cos 2\phi_T$ (left panel) and $\cos 2(\phi_T - \phi_\perp)$ (right panel) azimuthal asymmetries in the $e + p \to e + D +$ jet $+ X$ process as a function of y for $\sqrt{s} = 45$ GeV at fixed values of $z_h = 0.3$, $K_\perp = 2$ GeV for two values of $Q^2 = 10, 20$ GeV^2. The z and q_T are integrated over $0 < z < 1$, $0 < q_T < 1$ GeV.

$Q^2 = 20$ GeV^2 and at $y \approx 0.85$ for $Q^2 = 10$ GeV^2) and then becomes negative. As discussed above, this behavior is due to a relative dominance of the contributions from the transversely and longitudinally polarized photon. In the limit $y \to 1$, the $\cos 2\phi_T$ azimuthal asymmetry vanishes since the coefficient $\mathcal{B}_0$ as given in Eq. (A4) vanishes in this limit. This happens because the contribution from the longitudinally polarized photon vanishes. For $\cos 2\phi_T$, only the longitudinally polarized photon contributes, whereas for $\cos 2(\phi_T - \phi_\perp)$, both the longitudinally and transversely polarized photon contribute. As $y \to 1$, the ratio of $\mathcal{B}_2/\mathcal{A}_0$ which probes the $\cos 2(\phi_T - \phi_\perp)$ asymmetry comes only from transversely polarized photons. As seen in the z_h dependent plots, $\cos 2(\phi_T - \phi_\perp)$ asymmetry is larger for lower value of Q^2, whereas $\cos 2\phi_T$ asymmetry is larger for higher value of Q^2.

In Fig. 10, the q_T variation is shown and is Gaussian in nature due to the parametrization of TMDs. Both the asymmetries show a maximum at $q_T \approx 0.7$ GeV. The position of the maximum is independent of Q^2, however, the magnitude depends on Q^2. The magnitude of $\cos 2\phi_T$ increases as the virtuality of the photon increases, whereas the magnitude of $\cos 2(\phi_T - \phi_\perp)$ decreases as Q^2 increases. Overall, from these plots one can see that the asymmetries are quite sizable in the kinematics of EIC, reaching about 20–25% in certain regions.

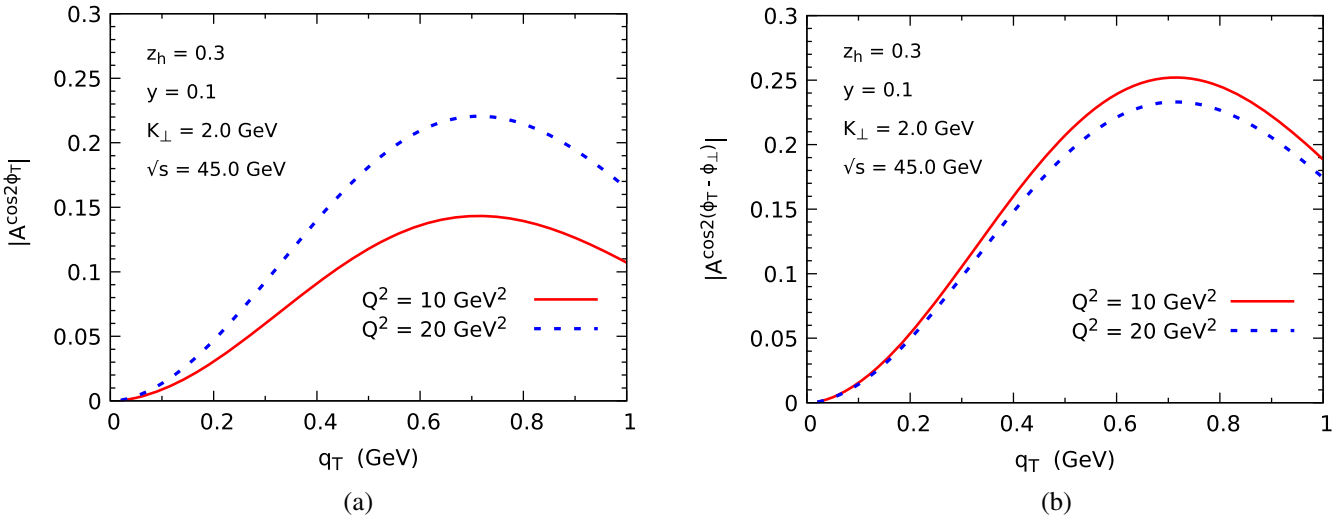

FIG. 10. Absolute values of $\cos 2\phi_T$ (left panel) and $\cos 2(\phi_T - \phi_\perp)$ (right panel) azimuthal asymmetries in the $e + p \to e + D +$ jet $+ X$ process as a function of q_T for $\sqrt{s} = 45$ GeV at fixed values of $K_\perp = 2$ GeV, $y = 0.1$ & $z_h = 0.3$ for two values of Q^2. The z is integrated over $0 < z < 1$.

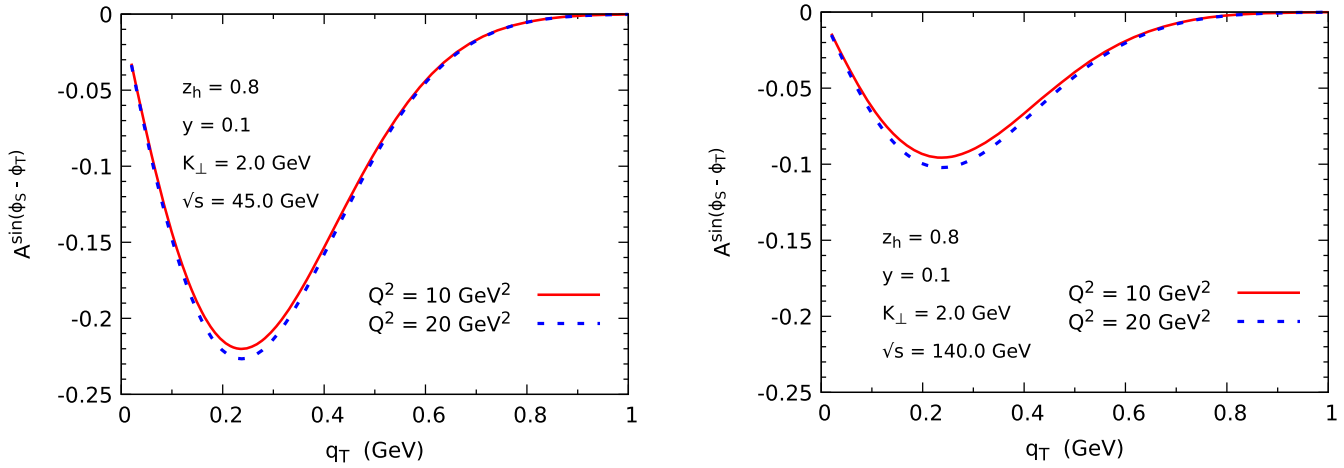

FIG. 11. Sivers asymmetry in the $e + p^\uparrow \to e + D + \text{jet} + X$ process as a function of q_T at fixed values of $y = 0.1$, $z_h = 0.8$, and $K_\perp = 2$ GeV for $\sqrt{s} = 45$ GeV (left panel) and $\sqrt{s} = 140$ GeV (right panel) for two values of Q^2. The z is integrated over $0 < z < 1$.

In Fig. 11, the Sivers asymmetry is shown at two different cm energies, $\sqrt{s} = 45$ GeV and $\sqrt{s} = 140$ GeV, respectively, for two different virtualities of the photon, and a Gaussian parametrization for the gluon Sivers function. It is seen from the plot that the Sivers asymmetry is negative. The asymmetry is quite sizable in our kinematics; for $\sqrt{s} = 45$ GeV the peak is about 23% whereas, for the higher energy, the peak is about 10%. The position of the peak is independent of the cm energy and is at $q_T \approx 0.2$ GeV for both energies. From Fig. 11, one can see that the Sivers asymmetry is high for a low cm energy, i.e., for $\sqrt{s} = 45$ GeV. This is due to the $\mathcal{N}_g(x)$ term of the Sivers function given in the Gaussian parametrization model. The $\mathcal{N}_g(x)$ term inversely depends on the cm energy through the x defined in Eq. (15). As cm energy increases, the x and $\mathcal{N}_g(x)$ decreases, which results in the decrease of the Sivers asymmetry. Additionally, one can see that the asymmetry does not depend that much on Q^2.

Figures 12 and 13 show the variation of Sivers asymmetry as a function of the inelasticity y and momentum fraction z_h for two different values of photon virtuality (Q^2) at two different cm energies ($\sqrt{s} = 45$ and 140 GeV). Here, the plots show the negative asymmetry. In Fig. 12, the magnitude of Sivers asymmetry decreases as the value of y increases. For y variation, the contribution from transversely polarized photons is significantly larger, approximately one order of magnitude higher, when compared to the contribution from longitudinally polarized photons.

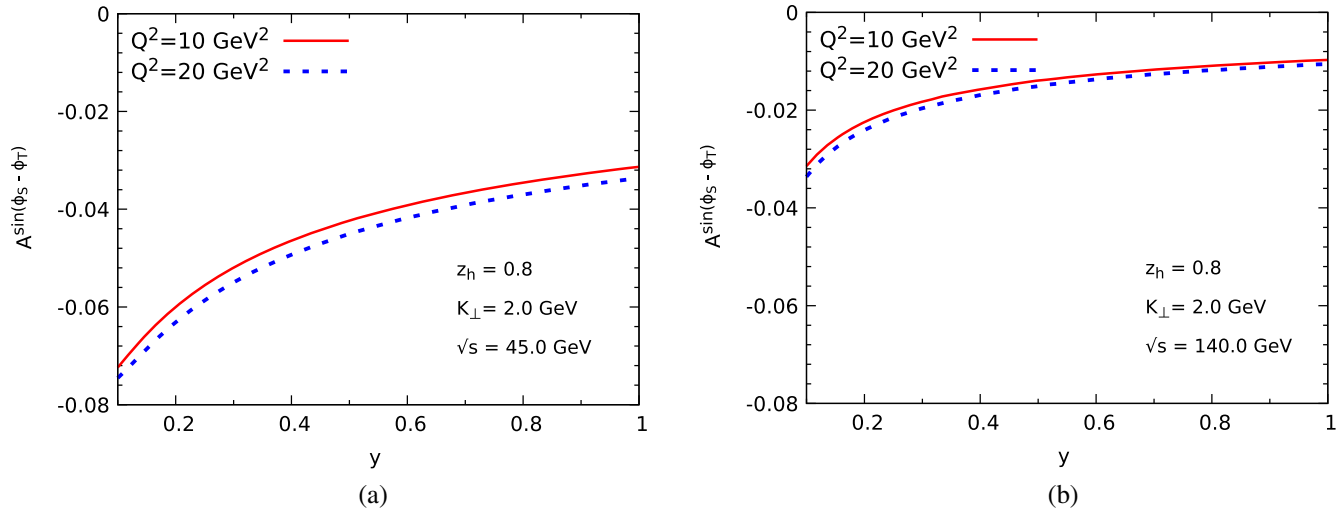

FIG. 12. Sivers asymmetry in the $e + p^\uparrow \to e + D + \text{jet} + X$ process as a function of y at fixed values of $K_\perp = 2.0$ GeV, $z_h = 0.8$ for $\sqrt{s} = 45$ GeV (left panel) and $\sqrt{s} = 140$ GeV (right panel) for two values of Q^2. The z and q_T are integrated over $0 < z < 1$, $0 < q_T < 1$ GeV.

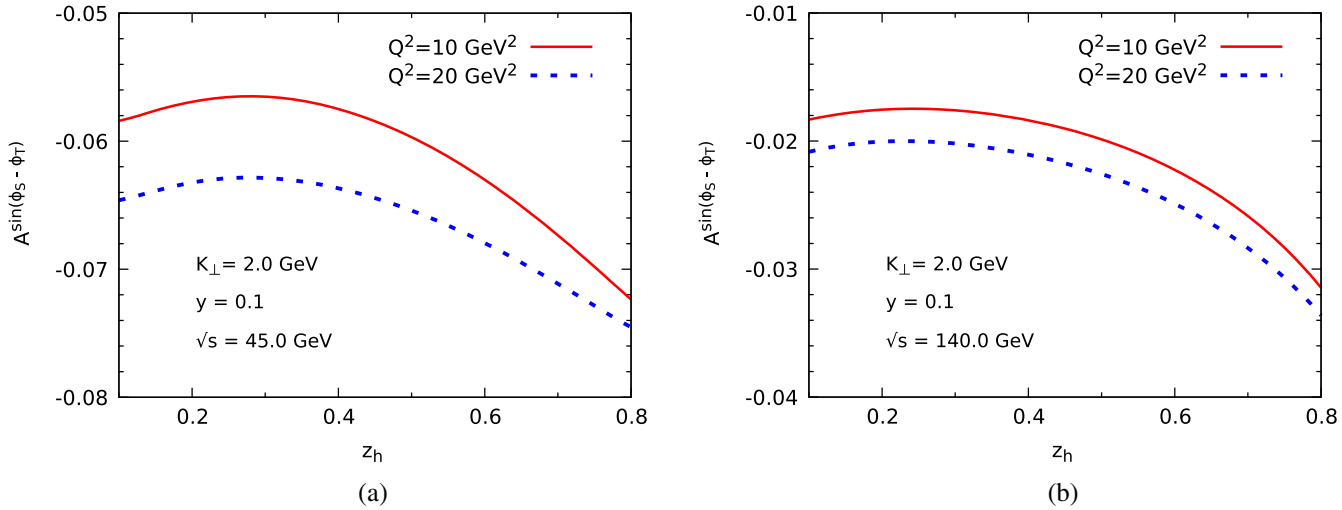

FIG. 13. Sivers asymmetry in the $e + p^\uparrow \to e + D + \text{jet} + X$ process as a function of z_h at fixed values of $K_\perp = 2.0$ GeV, $y = 0.1$ for $\sqrt{s} = 45$ GeV (left panel) and $\sqrt{s} = 140$ GeV (right panel) for two values of Q^2. The z and q_T are integrated over $0 < z < 1$, $0 < q_T < 1$ GeV.

This is observed throughout the range of y values; the transversely polarized photon contribution decreases as y increases. Notably, at $y = 1$, the contribution mainly comes from the transversely polarized photon, resulting in a nonvanishing asymmetry. The asymmetry does not depend significantly on the photon virtuality. In Fig. 13, both transversely polarized and longitudinally polarized photons contribute, with the transversely polarized photon making the dominant contribution. The magnitude of the Sivers asymmetry is maximum at $z_h = 0.8$, and it decreases for lower values of z_h. Furthermore, it is observed that the asymmetry is large for lower values of Q^2.

VI. CONCLUSION

In this article, we have investigated the azimuthal asymmetries in D-meson and jet production in the process of electron-proton collision in the kinematics of the future electron-ion collider. We have considered the kinematical condition where the final particles D meson and jet are almost back to back in the plane perpendicular to the direction of the incoming proton and the photon exchanged in the process, and we used the TMD factorization formalism. The D meson is produced from the fragmented charm quark in the photon-gluon fusion subprocess. We presented numerical estimates of the azimuthal asymmetries for this process; we calculated the model-independent upper bounds, as well as estimated the asymmetries using a widely used Gaussian parametrization of the TMDs. The $\cos 2\phi_T$ and $\cos 2(\phi_T - \phi_\perp)$ azimuthal modulations in the unpolarized cross section allow us to probe the linearly polarized gluon TMD. Our numerical estimates of the asymmetries in the kinematics of EIC show that they are sizable and can be as large as 20% in certain kinematical regions. The $\cos 2(\phi_T - \phi_\perp)$ shows a sign change due to competing contributions from transverse and longitudinally polarized virtual photons. When the proton is transversely polarized, we estimated the Sivers azimuthal modulation, $\sin(\phi_S - \phi_T)$, which could probe the gluon Sivers TMD. We obtained a sizable Sivers asymmetry in the kinematics considered, which will be accessible at the EIC. Our calculations show that D-meson and jet production at the EIC could be a useful process to probe the gluon TMDs.

ACKNOWLEDGMENTS

A. M. would like to thank SERB MATRICS (File No. MTR/2021/000103) for support. K. B. acknowledges support from Center for Frontiers in Nuclear Science (CFNS) through the joint IITB-CFNS postdoc position.

APPENDIX: AMPLITUDE MODULATIONS

We redefine the partonic Mandelstam variables as the following:

$$s = Q^2\left(\frac{x - x_B}{x_B}\right),$$
$$u = m_c^2 - z_1 x \frac{Q^2}{x_B},$$
$$t = m_c^2\left(\frac{z_1 - 1}{z_1}\right) + Q^2(z_1 - 1) - \frac{K_\perp^2}{z_1}.$$

The amplitude modulations are listed here:

$$\begin{aligned}\mathcal{A}_0 = &-\frac{1}{Q^2(Q^2+s)^2(m_c^2-u)^2(m_c^2-t)^2}\{(1+(1-y)^2)[3Q^{12}+4Q^{10}(5s+3(t+u))\\&+Q^8(53s^2+60s(t+u)+4(t^2+6tu+u^2))+4Q^6(18s^3+30s^2(t+u)+2s(3t+u)(t+3u)\\&-(t-u)^2(t+u))+Q^4(53s^4+120s^3(t+u)+48s^2(t+u)^2-4s(t-u)^2(t+u)+(t-u)^4)\\&+4Q^2s^2(5s^3+15s^2(t+u)+2s(5t^2+6tu+5u^2)+(t-u)^2(t+u))+s^2(3s^4+12s^3(t+u)\\&+4s^2(3t^2+2tu+3u^2)+4s(t-u)^2(t+u)+(t-u)^4)]+8(1-y)Q^2(m_c^2-u)(m_c^2-t)\\&\times[2Q^6+Q^4(5s+2(t+u))+4Q^2s(s+t+u)+s(s^2+2s(t+u)+(t-u)^2)]\},\end{aligned} \tag{A1}$$

$$\begin{aligned}\mathcal{A}_1 = &\frac{8\sqrt{1-y}(y-2)P_{hT}}{zQ(Q^2+s)(m_c^2-u)^2(m_c^2-t)^2}(t-u)[5Q^6+Q^4(13s+4(t+u))+Q^2(11s^2+8s(t+u)\\&-(t-u)^2)+s(3s^2+4s(t+u)+(t-u)^2)],\end{aligned} \tag{A2}$$

$$\begin{aligned}\mathcal{A}_2 = &\frac{4(y-1)}{Q^2(Q^2+s)^2(m_c^2-u)^2(m_c^2-t)^2}[(2Q^6+Q^4(5s+2(t+u))+4Q^2s(s+t+u)+s(s^2+2s(t+u)+(t-u)^2))\\&\times(3Q^6+2Q^4(4s+t+u)+Q^2(7s^2+4s(t+u)-(t-u)^2)+2s^2(s+t+u))],\end{aligned} \tag{A3}$$

$$\mathcal{B}_0 = \frac{y-1}{Q^2(Q^2+s)^2(m_c^2-u)^2(m_c^2-t)^2}(3Q^6+2Q^4(4s+t+u)+Q^2(7s^2+4s(t+u)-(t-u)^2)+2s^2(s+t+u))^2, \tag{A4}$$

$$\mathcal{B}_1 = \frac{2\sqrt{1-y}(y-2)(t-u)P_{hT}}{zQ(Q^2+s)(m_c^2-u)^2(m_c^2-t)^2}((3Q^6+2Q^4(4s+t+u)+Q^2(7s^2+4s(t+u)-(t-u)^2)+2s^2(s+t+u))), \tag{A5}$$

$$\begin{aligned}\mathcal{B}_2 = &-\frac{1}{Q^2(Q^2+s)^2(m_c^2-u)^2(m_c^2-t)^2}\{(1+(1-y)^2)(2Q^6+Q^4(5s+2(t+u))+4Q^2s(s+t+u)\\&+s(s^2+2s(t+u)+(t-u)^2))(Q^6+2Q^4(2s+t+u)+Q^2(5s^2+4s(t+u)-(t-u)^2)+2s^2(s+t+u))\\&+4(1-y)(m_c^2-u)(m_c^2-t)(2Q^6+Q^4(5s+2(t+u))+4Q^2s(s+t+u)+s(s^2+2s(t+u)+(t-u)^2))\},\end{aligned} \tag{A6}$$

$$\mathcal{B}_3 = \frac{2\sqrt{1-y}(y-2)(t-u)P_{hT}}{zQ(Q^2+s)(m_c^2-u)^2(m_c^2-t)^2}((2Q^6+Q^4(5s+2(t+u))+4Q^2s(s+t+u)+s(2u(s-t)+(s+t)^2+u^2))), \tag{A7}$$

$$\mathcal{B}_4 = \frac{y-1}{Q^2(Q^2+s)^2(m_c^2-u)^2(m_c^2-t)^2}(2Q^6+Q^4(5s+2(t+u))+4Q^2s(s+t+u)+s(2u(s-t)+(s+t)^2+u^2))^2. \tag{A8}$$

[1] P. J. Mulders and R. D. Tangerman, Nucl. Phys. **B461**, 197 (1996); **B484**, 538(E) (1997).

[2] D. Boer and P. J. Mulders, Phys. Rev. D **57**, 5780 (1998).

[3] A. Bacchetta, M. Diehl, K. Goeke, A. Metz, P. J. Mulders, and M. Schlegel, J. High Energy Phys. 02 (2007) 093.

[4] R. D. Tangerman and P. J. Mulders, Phys. Rev. D **51**, 3357 (1995).

[5] S. Arnold, A. Metz, and M. Schlegel, Phys. Rev. D **79**, 034005 (2009).

[6] M. G. A. Buffing, A. Mukherjee, and P. J. Mulders, Phys. Rev. D **88**, 054027 (2013).

[7] L. McLerran and R. Venugopalan, Phys. Rev. D **59**, 094002 (1999).
[8] Y. V. Kovchegov and A. H. Mueller, Nucl. Phys. **B529**, 451 (1998).
[9] F. Dominguez, J.-W. Qiu, B.-W. Xiao, and F. Yuan, Phys. Rev. D **85**, 045003 (2012).
[10] M. Bury, A. Prokudin, and A. Vladimirov, J. High Energy Phys. 05 (2021) 151.
[11] M. Boglione, U. D'Alesio, C. Flore, and J. O. Gonzalez-Hernandez, J. High Energy Phys. 07 (2018) 148.
[12] M. Anselmino, M. Boglione, U. D'Alesio, F. Murgia, and A. Prokudin, J. High Energy Phys. 04 (2017) 046.
[13] P. J. Mulders and J. Rodrigues, Phys. Rev. D **63**, 094021 (2001).
[14] S. Meißner, A. Metz, and K. Goeke, Phys. Rev. D **76**, 034002 (2007).
[15] D. W. Sivers, Phys. Rev. D **41**, 83 (1990).
[16] D. W. Sivers, Phys. Rev. D **43**, 261 (1991).
[17] X.-d. Ji, J.-P. Ma, and F. Yuan, Nucl. Phys. **B652**, 383 (2003).
[18] J.-w. Qiu and G. F. Sterman, Phys. Rev. D **59**, 014004 (1999).
[19] J.-w. Qiu and G. F. Sterman, Phys. Rev. Lett. **67**, 2264 (1991).
[20] J. C. Collins, Phys. Lett. B **536**, 43 (2002).
[21] S. J. Brodsky, D. S. Hwang, and I. Schmidt, Phys. Lett. B **530**, 99 (2002).
[22] A. V. Belitsky, X. Ji, and F. Yuan, Nucl. Phys. **B656**, 165 (2003).
[23] X.-d. Ji and F. Yuan, Phys. Lett. B **543**, 66 (2002).
[24] D. Boer, P. J. Mulders, and F. Pijlman, Nucl. Phys. **B667**, 201 (2003).
[25] A. Airapetian, N. Akopov, Z. Akopov, M. Amarian, A. Andrus, E. C. Aschenauer, W. Augustyniak, R. Avakian, A. Avetissian, E. Avetissian *et al.* (The HERMES Collaboration), Phys. Rev. Lett. **94**, 012002 (2005).
[26] A. Airapetian *et al.* (HERMES Collaboration), Phys. Rev. Lett. **84**, 4047 (2000).
[27] V. Y. Alexakhin *et al.* (COMPASS Collaboration), Phys. Rev. Lett. **94**, 202002 (2005).
[28] C. Adolph, M. Alekseev, V. Alexakhin, Y. Alexandrov, G. Alexeev, A. Amoroso, A. Antonov, A. Austregesilo, B. Badełek, F. Balestra *et al.*, Phys. Lett. B **717**, 383 (2012).
[29] U. D'Alesio, F. Murgia, and C. Pisano, J. High Energy Phys. 09 (2015) 119.
[30] U. D'Alesio, C. Flore, F. Murgia, C. Pisano, and P. Taels, Phys. Rev. D **99**, 036013 (2019).
[31] A. Adare *et al.* (PHENIX Collaboration), Phys. Rev. D **90**, 012006 (2014).
[32] D. Boer, S. J. Brodsky, P. J. Mulders, and C. Pisano, Phys. Rev. Lett. **106**, 132001 (2011).
[33] C. Pisano, D. Boer, S. J. Brodsky, M. G. A. Buffing, and P. J. Mulders, J. High Energy Phys. 10 (2013) 024.
[34] A. V. Efremov, N. Y. Ivanov, and O. V. Teryaev, Phys. Lett. B **777**, 435 (2018).
[35] D. Chakrabarti, R. Kishore, A. Mukherjee, and S. Rajesh, Phys. Rev. D **107**, 014008 (2023).
[36] U. D'Alesio, F. Murgia, C. Pisano, and P. Taels, Phys. Rev. D **100**, 094016 (2019).
[37] R. Kishore, A. Mukherjee, A. Pawar, and M. Siddiqah, Phys. Rev. D **106**, 034009 (2022).
[38] R. Kishore, A. Mukherjee, and S. Rajesh, Phys. Rev. D **101**, 054003 (2020).
[39] R. Kishore and A. Mukherjee, Phys. Rev. D **99**, 054012 (2019).
[40] R. Kishore, A. Mukherjee, and M. Siddiqah, Phys. Rev. D **104**, 094015 (2021).
[41] U. D'Alesio, L. Maxia, F. Murgia, C. Pisano, and S. Rajesh, J. High Energy Phys. 03 (2022) 037.
[42] U. D'Alesio, L. Maxia, F. Murgia, C. Pisano, and S. Rajesh, Phys. Rev. D **102**, 094011 (2020).
[43] S. Rajesh, R. Kishore, and A. Mukherjee, Phys. Rev. D **98**, 014007 (2018).
[44] J.-W. Qiu, M. Schlegel, and W. Vogelsang, Phys. Rev. Lett. **107**, 062001 (2011).
[45] D. Boer and C. Pisano, Phys. Rev. D **91**, 074024 (2015).
[46] R. M. Godbole, A. Kaushik, and A. Misra, Phys. Rev. D **97**, 076001 (2018).
[47] M. Anselmino, M. Boglione, U. D'Alesio, E. Leader, and F. Murgia, Phys. Rev. D **70**, 074025 (2004).
[48] R. M. Godbole, A. Kaushik, and A. Misra, Phys. Rev. D **94**, 114022 (2016).
[49] U. D'Alesio, F. Murgia, C. Pisano, and P. Taels, Phys. Rev. D **96**, 036011 (2017).
[50] Z.-B. Kang and J.-W. Qiu, Phys. Rev. D **78**, 034005 (2008).
[51] Y. Koike, K. Tanaka, and S. Yoshida, Phys. Rev. D **83**, 114014 (2011).
[52] D. Boer, P. J. Mulders, C. Pisano, and J. Zhou, J. High Energy Phys. 08 (2016) 001.
[53] A. Bacchetta, M. Boglione, A. Henneman, and P. J. Mulders, Phys. Rev. Lett. **85**, 712 (2000).
[54] B. A. Kniehl and G. Kramer, Phys. Rev. D **74**, 037502 (2006).
[55] A. D. Martin, W. J. Stirling, R. S. Thorne, and G. Watt, Eur. Phys. J. C **63**, 189 (2009).
[56] D. Boer, W. J. den Dunnen, C. Pisano, M. Schlegel, and W. Vogelsang, Phys. Rev. Lett. **108**, 032002 (2012).
[57] D. Boer and C. Pisano, Phys. Rev. D **86**, 094007 (2012).
[58] A. Bacchetta, U. D'Alesio, M. Diehl, and C. A. Miller, Phys. Rev. D **70**, 117504 (2004).
[59] M. Anselmino, M. Boglione, U. D'Alesio, A. Kotzinian, F. Murgia, and A. Prokudin, Phys. Rev. D **72**, 094007 (2005); **72**, 099903(E) (2005).